Cell Reports
Physical Science

CellPress
OPEN ACCESS

Article

Lithium deposition in single-ion conducting polymer electrolytes

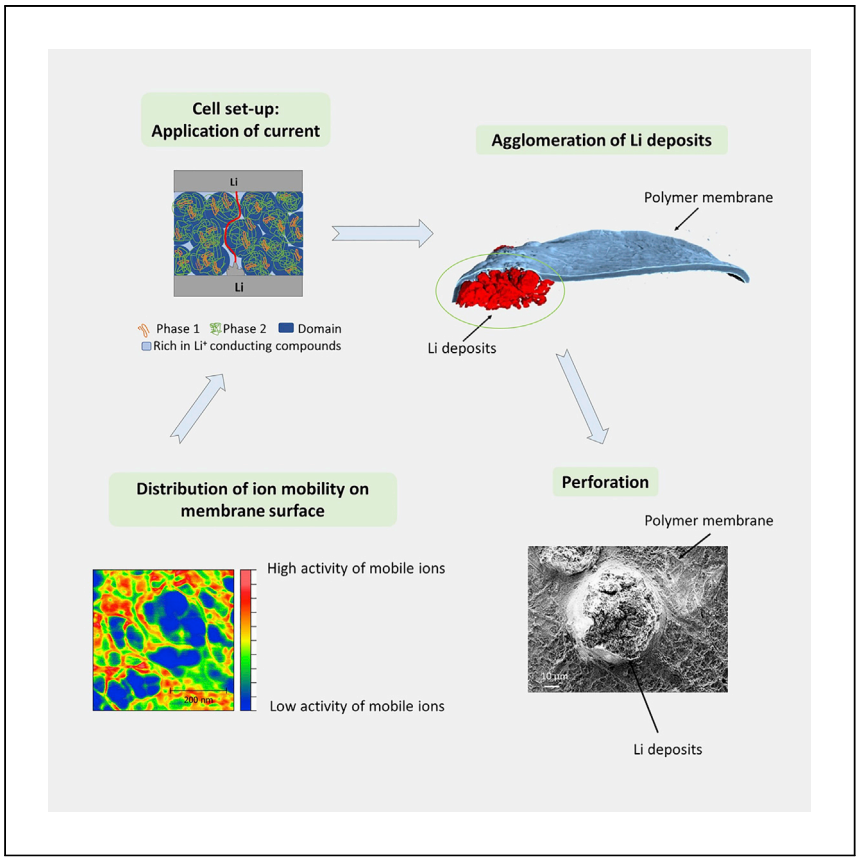

Combined galvanostatic cycling, scanning electron microscopy, and X-ray tomography imaging techniques are applied by Borzutzki et al. They reveal the impact of microstructural electrolyte features on the Li deposition behavior in a single-ion conducting blend-type polymer electrolyte, thereby identifying a previously neglected critical parameter for future electrolyte design and subsequent control of Li deposition.

Kristina Borzutzki, Kang Dong, Jijeesh Ravi Nair, ..., Martin Winter, Ingo Manke, Gunther Brunklaus

manke@helmholtz-berlin.de (I.M.)
g.brunklaus@fz-juelich.de (G.B.)

Highlights

Li deposition in single-ion conducting polymer cells is analyzed in various ways

Agglomeration of dense Li deposits/deformation of the polymer membrane observed

Microphase separation in electrolytes induces preferential Li^+ transport paths

Electrolyte morphology is revealed as critical parameter for Li deposition behavior

Borzutzki et al., Cell Reports Physical Science 2, 100496
July 21, 2021 © 2021 The Author(s).
https://doi.org/10.1016/j.xcrp.2021.100496

Cell Reports
Physical Science

CellPress
OPEN ACCESS

Article

Lithium deposition in single-ion conducting polymer electrolytes

Kristina Borzutzki,[1,7] Kang Dong,[2,3,7] Jijeesh Ravi Nair,[1] Beatrice Wolff,[4,5] Florian Hausen,[4,5] Rüdiger-A. Eichel,[4,5] Martin Winter,[1,6] Ingo Manke,[3,*] and Gunther Brunklaus[1,8,*]

SUMMARY

Lithium (Li)-metal is considered as promising anode material for high-energy-density rechargeable batteries, although its application is hampered by inhomogeneous Li deposition and dendritic Li morphologies that could eventually result in contact losses of bulk and deposited Li as well as cell short circuits. Based on theoretical investigations, recent works on polymer electrolytes particularly focus on the design of single-ion conducting electrolytes and improvement of bulk Li^+ transport properties, including enhanced Li^+ transference numbers, ionic conductivity, and mechanical stability, thereby affording safer and potentially "dendrite-free" cycling of Li-metal batteries. In the present work, it is revealed that the spatial microstructures, localized chemistry, and corresponding distributions of properties within the electrolyte are also decisive for achieving superior cell performances. Thus, targeted modification of the electrolyte microstructures should be considered as further critical design parameters for future electrolyte development and to actually control Li deposition behavior and longevity of Li-metal batteries.

INTRODUCTION

Lithium (Li)-metal is considered as the most promising anode material, mainly due to its high theoretical capacity (3,860 mAh · g^{-1}) compared to the lithiated graphite anode (339 mAh · g^{-1}) applied in Li-ion batteries,[1–4] despite the reliable control of inhomogeneous Li-metal deposition remaining a major challenge.[5,6] To address these challenges, numerous experimental and theoretical studies explored relevant features of Li deposition/stripping mechanisms, while theoretical work identified critical parameters and preferred conditions that may enable long-term cycling of Li-metal batteries (LMBs).

In Chazalviel's model[7] the deposition of high surface area Li (HSAL) correlates with salt anion mobility, so that the growth of dendritic Li will be unavoidable upon anion depletion at the negative electrode interface. Here, electrolytes affording high Li^+ diffusivity (D_{Li+}) and a Li^+ transference number (t_+) close to 1 (single-ion conductor) are expected to reduce or even prevent the formation of "dendritic" Li.

Also, the shear modulus (G) of polymer electrolytes (representing mechanical features of the material) is emphasized as a relevant parameter.[8,9] It was proposed that G should be at least two times higher than that of Li-metal to circumvent materials penetration by Li deposits, implying an electrolyte shear moduli of $G > 6$ GPa.[8] Thus, solid-state electrolytes comprising polymers, ceramics, or hybrids appear highly promising for practical application in LMBs. However, recent experimental

[1]Helmholtz-Institute Münster, IEK-12, Forschungszentrum Jülich GmbH, 48149 Münster, Germany

[2]Institute of Materials Science and Technology, Technische Universität Berlin, Straße des 17. Juni, 10623 Berlin, Germany

[3]Helmholtz-Zentrum Berlin für Materialien und Energie, Hahn-Meitner-Platz 1, 14109 Berlin, Germany

[4]IEK-9, Forschungszentrum Jülich, 52425 Jülich, Germany

[5]RWTH Aachen University, Institute of Physical Chemistry, 52074 Aachen, Germany

[6]University of Münster, MEET Battery Research Center, Institute of Physical Chemistry, 48149 Münster, Germany

[7]These authors contributed equally

[8]Lead contact

*Correspondence: manke@helmholtz-berlin.de (I.M.), g.brunklaus@fz-juelich.de (G.B.)

https://doi.org/10.1016/j.xcrp.2021.100496

This is an open access article under the CC BY-NC-ND license (http://creativecommons.org/licenses/by-nc-nd/4.0/).

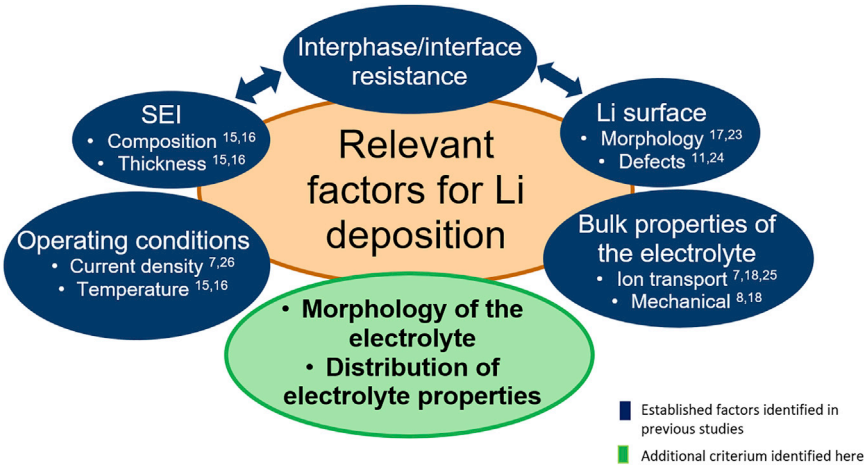

Figure 1. Critical parameters determining Li deposition behavior

Presentation of relevant parameters influencing Li deposition behavior already established by previous investigations (blue symbols) and additional parameters that are identified in this work (green symbol).

studies pointed out that even then inhomogeneous growth of lithium deposits could induce cell failures originating from local defects, triggering the growth of Li deposits within "hotspots,"[10,11] while cross-linked systems even with low modulus (0.1 MPa) may efficiently prevent the penetration of dendritic Li.[12] Therefore, the original Chazalviel model was extended, taking into account the intercorrelations of mechanical and ion transport properties, revealing that the utilization of polymers with immobilized anions likely fosters stable electro-deposition even in cases of moderate shear moduli (in the MPa range) of the electrolytes.[13] Despite that a quantitative comparison to experimental results could not be performed, mainly due to limited systematic experimental investigations of (quasi-) solid electrolytes, order-of-magnitude estimates exploiting the limited data for the required model parameters unambiguously demonstrated consensus between the proposed theory and considered experiments.

Models often assume ideal interfaces despite that in "real" cell systems, interphase characteristics have an essential impact on Li deposition, in which the actual morphology of Li deposits strongly correlates with interphase characteristics (e.g., Li surface roughness, solid electrolyte interphase [SEI] composition), as well as cell operating conditions (e.g., cycling current, temperature) and electrolyte properties.[14–18] Experimental observations mainly cover the case of liquid electrolytes while in the case of (single-ion conducting) polymer-based electrolytes, only a few studies provide systematic analyses of Li deposition, rendering limiting factors and conditions (correlated to, e.g., Chazalviel's model) ambiguous and ill-defined. In this respect, extensive further experimental efforts are required to identify all of the relevant parameters and complex relations between SEI formation, the nature of (solid) electrolytes, and Li-metal (surface) properties that govern observable Li-metal deposition.

Considering the parameters that have been identified as critical for Li deposition behavior, particularly electrolyte properties (ionic conductivity, Li^+ transference number, modulus), Li electrode surface characteristics, SEI properties and operating conditions of the cell, (summarized in Figure 1, blue symbols), here, the fundamental aspects of Li deposition phenomena in symmetric Li | SIPE | Li cells and data

correlation to model-based predictions are described. A blend polymer membrane composed of aromatic polysulfonamide-based single-ion conducting compounds, a flexible linear polymer (poly(vinylidene difluoride-co-hexafluoropropylene) [PVdF-HFP]) and carbonate-based plasticizers, affording excellent bulk properties, including an ionic conductivity of 1 mS cm^{-1} at 60°C, ion diffusivity of $D_{Li+} \approx 10^{-11}$ m^2s^{-1}, single-ion conducting behavior ($t_{+,Li}$ = 0.9), and a moderate elastic modulus of $G \approx 10^5$ Pa is studied.

Li deposition was conducted at different current rates but with constant deposition capacity, followed by imaging characterization of scanning electron microscopy (SEM) and synchrotron X-ray tomography. Independent of applied current densities, Li deposits tend to grow in particular spots unevenly across the Li anode. Induced by rather high growth rates at these spots,[16,19] high mechanic pressure may accumulate that could eventually lead to strong deformation and thinning of the polymer membrane, if not even to its perforation.

The chemical composition of the polymer membranes is monitored by Raman mapping, corroborating the inhomogeneous distribution of constituents due to phase separation and agglomeration of the domains. In addition, quantitative nano-mechanical (QNM) and electrochemical strain microscopy (ESM) mapping reveal the presence of a distribution of stiffness (variation of Young's modulus between <1 and 80 MPa) and ionic mobility/flow within the membrane. The analysis suggests that the intrinsic nature of the considered polymer blend membrane is responsible for the formation of favored conduction channels triggering inhomogeneous Li deposition.

Despite that the impact of polymer membrane morphology on the achievable ion transport properties, distribution of solvation paths in polyethylene oxide (PEO)-based electrolytes[20], structure-transport correlation in block copolymers,[21] or anisotropy of diffusion coefficients in blend PVdF/polyelectrolytes for fuel cells[22] is reported, membrane homogeneity as a potential design parameter of polymer electrolytes that enable homogeneous Li deposition was typically neglected. Therefore, the impact of (rather localized) variation of polymer properties on the nature of resulting Li deposits is explored in this work, in which membrane morphology and homogeneity are introduced as additional crucial parameters that significantly determine the Li deposition behavior (illustrated as green symbol in Figure 1).

RESULTS AND DISCUSSION

Li deposition at varying surface conditions of Li-metal electrodes

Surface properties of Li electrodes significantly control the Li deposition behavior and the cycling stability of Li-metal-based cells (Figure 1). Specifically, Li nucleation preferentially starts at surface defects as a result of high local Li-ion flux in liquid-electrolyte systems.[23,24] Therefore, surficial pre-treatment of the metal anode, explicitly surface modification of the Li-metal as well as the initial oxidation layer thereon, is critical to reveal the Li deposition behavior, but is rarely reported even in liquid-electrolyte systems.[24–30]

In addition to the as-received Li-metal, hexane washed[25,31,32] and roll-pressed[26] Li-metal electrodes were prepared to explore the Li deposition under different surface conditions. Hexane constitutes a suitable solvent for Li treatment since it is inert toward metallic Li but dissolves various organic compounds. Notably, SEM images (Figures 2A–2C) indicate that hexane washing did not alter the surface roughness, while X-ray photoelectron spectroscopy (XPS) data in Figure 2D and Table 1 (spectra

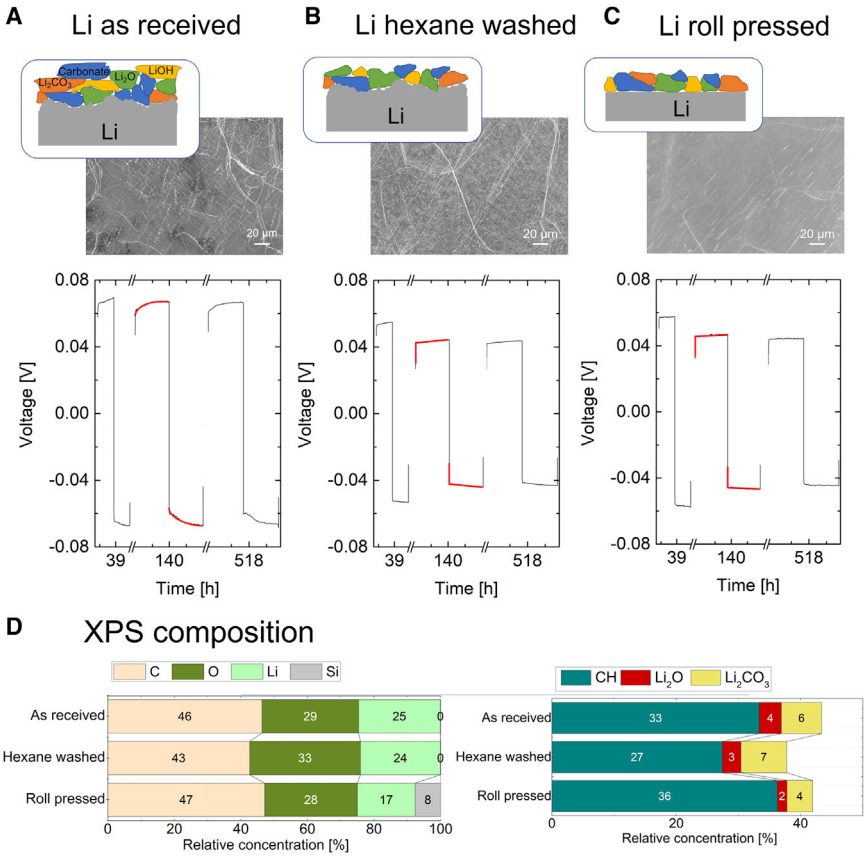

Figure 2. Influence of different Li-metal treatments on the surface properties

(A–C) SEM. Li surface image, schematic of Li surface and SEI composition (based on SEM and XPS measurements) and overvoltage profiles for selected cycles of stripping/plating investigations performed on (A) as-received, (B) hexane washed, and (C) roll-pressed Li-metal anodes. A current density of 0.2 mA cm^{-2} was applied for 1 h in the first cycles (t = 38–40 h) and for 2 h during later cycles, reflecting deposited Li amounts of 0.046 and 0.092 mg, respectively.

(D) XPS composition of the Li surfaces.

are presented in Figure S3) exhibit the removal of contaminated hydrocarbons[26] from the Li surface upon washing, as reflected by (slightly) lower contents of hydrocarbon compounds and carbon species. In contrast, roll-pressing could remarkably decrease the surface roughness (SEM) and the content of the surficial Li salts (i.e., Li_2O and Li_2CO_3) by 56.6% and 36.4% (XPS; Table 1), respectively, thus improving surface structural and chemical homogeneity of the Li.

Stripping/plating and electrochemical impedance spectroscopy (EIS; Figure S4) were performed using Li|SIPE (single-ion conducting polymer electrolyte)|Li symmetric cells to evaluate the effects of Li treatment on the electrochemical behavior. In contrast to a high fluctuation of voltage plateaus in liquid-electrolyte-based cells,[26] all Li|SIPE|Li symmetric cells show stable voltage profiles during 130 cycles (total charge: C = 367.2 C cm^{-2}) of the experiment (Figure S4), thereby demonstrating an improved cycling stability using SIPE.

The major difference appears in the voltage profiles of half-cycles as shown in Figure 2 for several representative cycles. The highest value of overvoltage of 67 mV at 0.2 mA cm^{-2} (at t = 139 h) is observed in the case of as-received Li-metal

Table 1. at% of the compounds detected on the differently treated Li-metal electrodes by XPS

	Li_2O (O 1 s)		Li_2CO_3 (C 1 s)		CH ($C_{1\ s}$)		C		Li	
	Content (at%)	Variation (%)	Content (at%)	Variation (%)	Content (at%)	Variation (%)	Content (at%)	Variation (%)	Content (at%)	Variation (%)
Li as-received	3.6 ± 0.1	N/A	6.5 ± 0.4	N/A	33.3 ± 1.5	N/A	45.5 ± 1.2	N/A	24.1 ± 0.5	N/A
Hexane washed	3.0 ± 0.3	−15.7	7.4 ± 0.4	13.6	27.4 ± 1.2	−17.8	41.3 ± 0.8	−9.3	23.3 ± 0.6	−3.4
Roll-pressed	1.6 ± 0.2	−56.6	4.1 ± 0.4	−36.4	36.3 ± 0.6	8.7	43.4 ± 1.2	−4.7	16.0 ± 0.2	−33.7

Variations relate to the value of as-received Li. at%, atomic concentration; XPS, X-ray photoelectron spectroscopy.

(Figure 2A). The lower overvoltage observed in cells using hexane-washed (44 mV; Figure 2B) and roll-pressed (42 mV; Figure 2C) Li-metal illustrates an improved cycling performance after the surface modification of Li.

In addition, as indicated by red lines in Figures 2A–2C, an arcing behavior of the actual overvoltage can be observed in all cycles in the case of the as-received Li-metal. A change in overvoltage is attributed to polarization effects, often observed in dual-ion conductors as a result of an anion concentration gradient along the cell,[33–35] but it is not expected in a SIPE.

For evaluation and comparison of interfacial resistances of the impedance spectra (Figure S3), a combined electrolyte and interface resistance R_{EL}+R_{SEI} was considered since the limited amount of data points collected in the high-frequency region (f > 100 kHz, reflecting SEI (R_{SEI}) and bulk electrolyte (R_{EL}) resistances) inhibited unambiguous separation of both contributions. Thus, assuming a constant electrolyte resistance R_{EL}—or at least constant change of R_{EL} over time, independent of the Li treatment—occurring changes in R_{EL}+R_{SEI} are assigned to variations in R_{SEI} only. Comparing the different procedures of Li treatment, a smaller value of R_{EL}+R_{SEI} (104 and 79 Ω; Figure S4D) of cells with pre-treated Li, compared to cells using as-received Li-metal anodes (158 Ω), indicate decreased interphase resistance, thereby corroborating (partial) removal of surface oxidation layers by both treatments. This further affects the overvoltage profile, in which no arcing behavior is observed for pre-treated samples. The overvoltage profile of cells with Li anodes that were washed slightly increases during each half-cycle, likely due to changes in the SEI characteristics, whereas only the roll-pressed Li exhibits the anticipated flat voltage plateau. The exact values of determined SEI resistances vary significantly based on the type of Li foil (e.g., manufacturer, storage conditions) that is used and materials combinations (e.g., type and chemical contribution of the electrolyte). Previous studies on other SIPE-based symmetric Li||Li cells report values for R_{SEI} ranging from 20 to 1,000 Ω[36–39]; thus, a comparison of R_{SEI} between different studies is rather meaningless, while trends within the same study can readily identify strategies for interphase optimization. Based on the Li-metal treatments considered here, it is emphasized that roll-pressing affords Li electrode surfaces with high structural and chemical homogeneity, thereby avoiding undesirable polarization phenomena at the interphase.

Li deposition behavior with SIPE

Since roll-pressed Li-metal facilitates superior electrochemical performance in the case of SIPE, it is used to analyze details of the Li deposition in SIPE-based cells, particularly invoking a previously introduced single-ion conducting blend polymer electrolyte, applied in NMC111||Li full cells for long-term cycling.[40] A high ionic

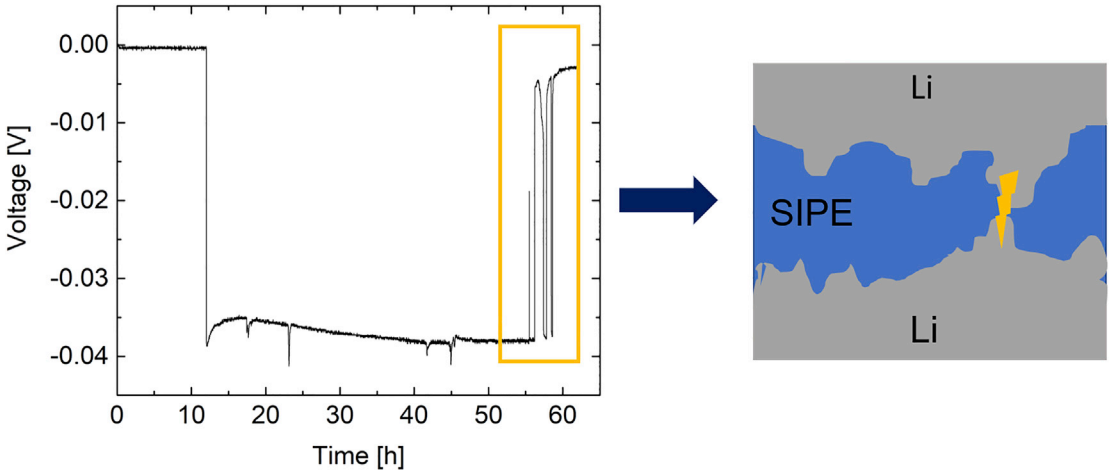

Figure 3. Experimental determination of the short-circuit time

Continuous single-side deposition performed in a symmetric Li||Li cell (0.1 mA cm^{-2}) until a short circuit of the cell occurs.

conductivity of 1.1 mS cm^{-1} at 60°C was obtained, while the Li-ion transference number determined by the Bruce-Vincent method[41] amounts to 0.9.[40] Based on the determined Li^+ transport properties, the corresponding short-circuit time τ_{SC} of the SIPE is estimated based on Chazalviel's model (details of the model are described in Data S1 and Table S1), assuming a single-sided deposition at a current density of 0.1 mA cm^{-2}, while yielding a short-circuit time of 826 h that, in principle, suggests excellent durability of SIPE-based Li-metal cells.

Continuous Li deposition was performed in a symmetric Li||Li cell. While a few voltage spikes occur during plating probably related to micro-short-circuits induced as Li deposits immediately lose contact, a sudden drop of the overvoltage (to ~0 V), as indicated by the yellow box in Figure 3, represents shortening of the cell. The experimentally obtained value for τ_{SC} equals 43 h, which is far below the theoretical value (826 h). Such a large discrepancy between the estimated and experimental values is unexpected.

To elucidate the likely cause for this fast cell failure, Li deposition was studied by SEM and synchrotron X-ray tomography. SEM permits the investigation of the initial stages of Li deposition at the nanometer range, while X-ray tomography, as a non-destructive and non-invasive method, was used to unravel the three-dimensional (3D) microstructure and spatial distribution of Li deposits without altering the chemistry and morphology of the Li|SIPE interphase in the micrometer range (with 1.2 μm spatial resolution). Before post-mortem imaging, single-side deposition in Li||Li cells was done at different current rates with a fixed amount of charge passed C = 7.2 C cm^{-2}, corresponding to 0.46 mg Li. The individual voltage profiles are presented in Figure S5. Figure 4 shows the SEM images of the Li-metal anode (Figure 4A) and the polymer membrane (Figure 4B) on the side where Li deposition occurred as well as representative cross-sectional and 3D-rendered images obtained by X-ray tomography (Figures 4C and 4D, respectively; videos of the complete tomograms are attached as Videos S1, S2, and S3). On the Li-metal anode side, merely few deposits (non-agglomerated deposits of <100 nm; Figure S6) adhere (Figure 4A), whereas large agglomerates stick to the polymer electrolyte when disassembling the cell, which is independent of the applied current density (Figure 4B). The deposits are non-dendritic, but densely packed "mossy" structures. The agglomeration of Li deposits is in good agreement with initial

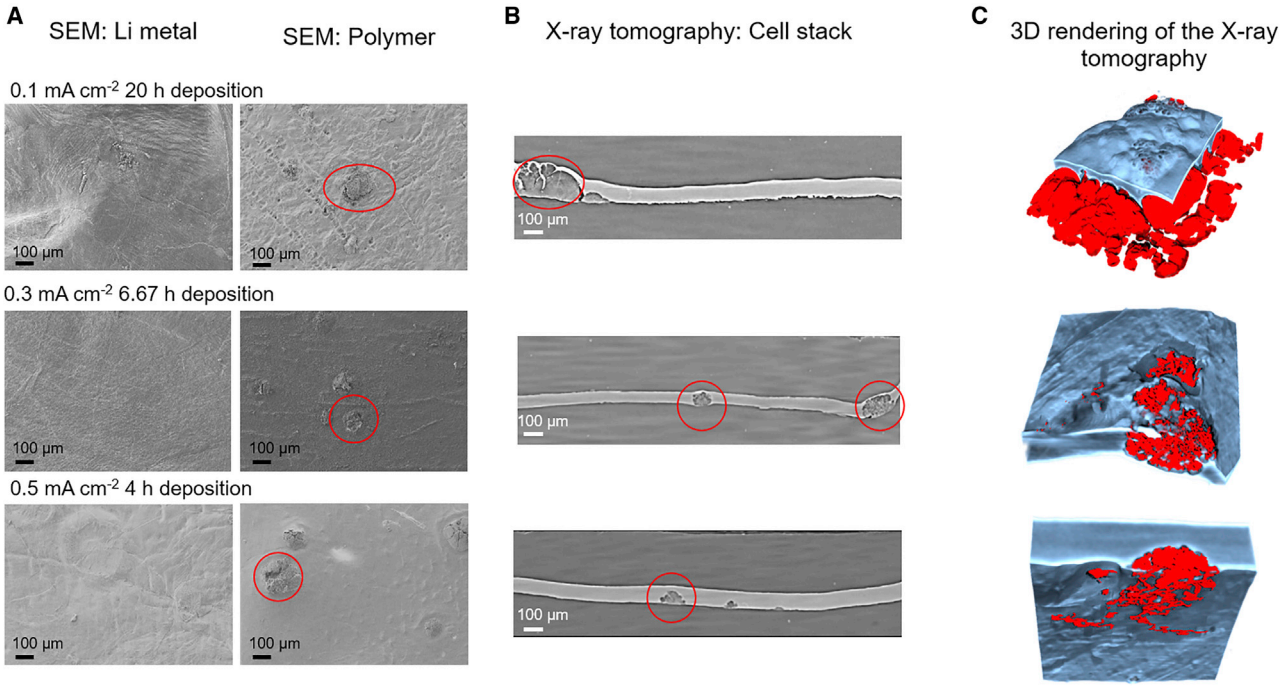

Figure 4. Post-mortem imaging analysis of Li deposits

Presented cells were cycled at different currents but with a fixed amount of charge of 7.2 C cm^{-2} (≙ 46 mg Li).

(A and B) SEM images of the Li-metal electrode (on which Li was plated, A) and polymer membranes (B) after single-side deposition.

(C) Cross-sectional views from X-ray tomography showing distribution of Li deposits.

(D) 3D rendering of sub-datasets from X-ray tomography revealing the morphology and spatial distribution of Li deposits (red) with SIPE (light blue).

deposition at preferential spots from which they begin to deform the membrane. This, in turn, results in an increased electric and ionic field and thus, an increase in current density at the tip of the deposited Li-metal,[9,16,19] yielding further deposition, deformation, and even thinning of the polymer membrane and eventual perforation of the polymer matrix due to rather high local stress.

Note that the observed behavior is not simply attributed to the rather low elastic modulus of the polymer membrane of 0.1 MPa (determined by rheometry; Figure S7). In previous studies, cross-linked PE/PEO systems with a similarly low modulus of 0.1 MPa, significantly lower transference number (t^+ = 0.16), and similar ionic conductivity at cycling temperature[42] compared to the SIPE considered here, achieved short-circuit times that exceed the value predicted by Chazalviel's model. In addition, a recent study demonstrated that a single-phase elastic salt-containing quasi-solid polymer electrolyte with a modulus of only 0.4 MPa efficiently prevents cell failure by the penetration of Li deposits even at high current rates.[43] This was ascribed to the relation between the modulus and density of highly porous structures, implying that the shear modulus of deposited mossy (porous) Li is reduced to the megapascal level compared to 3.4 GPa (for dense Li-metal), thereby substantially reducing the actually required modulus of (polymer) electrolytes.[44] Therefore, it can be concluded that polymer membrane elasticity was not the limiting factor, and may even be sufficient to prevent cell failure, provided that Li deposition occurs homogenously. Nonetheless, the observed non-homogeneous deposition behavior limits the electrochemical performance of the applied polymer membrane despite its excellent bulk transport properties.

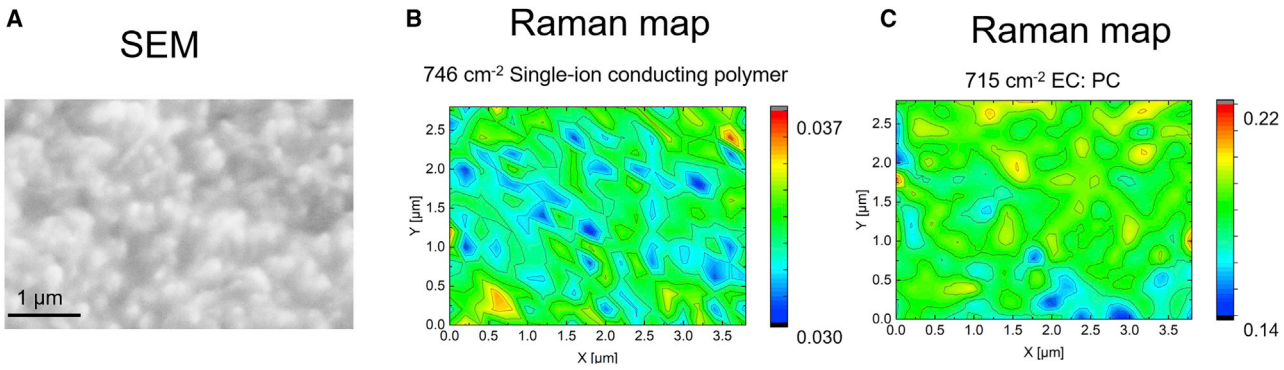

Figure 5. Surface characterization of the SIPE membrane
(A–C) (A) SEM and (B and C) Raman mapping of the SIPE and solvent solution.

Membrane morphology and its correlation to Li deposition

For (quasi) solid blend polymer membranes or block copolymers, a well-known and intended design strategy comprises the phase separation of different compounds on the nanometer scale. A separation of the Li salt solvating polymer block combined with a mechanically stiffer compound enables the formation of continuous pathways for ion transport, while ensuring mechanical stability. Therefore, the favored bulk ion transport and mechanical properties compared to, for example, homopolymers or polymers composed of a single compound can be obtained.[45,46] In addition, clustering of different phases and formation of larger nodules (agglomerates) has been reported,[47–49] while the impact of such behaviors on electrochemical cell performances has not been explored, and it was even expected that polymer electrolytes are generally uniform on the meso scale.[50] In our previous work,[51] it was revealed that for multi-compound systems, phase separation and clustering of domains occur on a nanometer scale, yielding crystalline PVdF-HFP and amorphous intermixed PVdF-HFP/SIPE phases, as well as solvent-rich and solvent-poor domains. As depicted in SEM images (Figure 5A), nanometer-size domains aggregate, resulting in structures on the order of several hundred nanometers; to highlight the impact and extent of phase separation, 2D analysis methods were invoked.

The chemical distribution of electrolyte constituents at the membrane surface is derived from Raman spectroscopy. Notably, mapping of characteristic Raman peaks at 746 cm^{-1} related to the anionic moiety within the polymer backbone[52] (Li-sulfonamide interactions) and at 715 cm^{-1} representing symmetric ring deformation of the solvent molecules,[53] is presented in Figure 5; the corresponding Raman spectra are shown in Figure S8. In view of a practical lateral resolution of ~500 nm and a penetration depth of <5 µm[54,55] under the applied conditions, the distribution of solvent and single-ion conducting polymer over the surface could be displayed. The domains with a size of ~200 nm (also compare to Borzutzki et al.[51]) are arranged in such a way that even within a larger detection volume, the signals (summation of compounds within a certain volume) do not yield identical contents of the compounds, clearly illustrating an inhomogeneous distribution of the single-ion conducting polymer as well as solvent within the polymer blend membrane. Note that the distribution of PVdF-HFP could not be analyzed reliably due to low signal intensity (Figure S9).

Infrared (IR) spectra (Figure S9) of the membranes yield stronger excitation of the corresponding vibration than Raman spectra and clearly show the presence of α, β, and γ phases of PVdF, of which only the β phase has piezoelectric behavior.[56–61] IR spectra

did not change noticeably upon swelling, drying, or cycling of the cells, indicating the high phase stability of these membranes. This is unlike other membrane treatments (e.g., mechanical or thermal treatment, embedding of additional compounds) that could change chain configurations of PVdF(-HFP).[58–61] Furthermore, in a previous study, the distribution of the different phases within a PVdF-HFP-based polymer electrolyte were mapped, revealing their inhomogeneous distribution over the membrane surface.[55] Thus, in addition to the distribution of single-ion conducting polymer and plasticizer (Figure 5B), the distribution of PVdF-HFP phases most probably constitutes a further inhomogeneity.

Based on the determined structural and compositional inhomogeneities, it is evident that the transport and mechanical properties also vary within the material. To corroborate this assumption, various modes of atomic force microscopy (AFM) were used, including QNM imaging for the local determination of Young's modulus and ESM[62,63] for the spatial mapping of ionic mobility/flow that is related to percolation paths in the polymer.[64] ESM is a rather novel and powerful technique that has been developed within the last several years to unravel electrochemical processes on the nanoscale by intrinsically linking electrochemical processes and strains.[65] Inducing a small alternating current (AC) bias to the probe locally (in the vicinity of the tip) redistributes the Li^+ ion concentration within the sample. This in turn results in a change in the molar volume of the sample that is identified by the electrochemical strain measured by the ESM probe. While various mechanisms may contribute to the observed strain, ESM probes ionic flows with outstanding resolution on a nanometer scale.[62,64–67] However, while being applied to various solid battery compounds, in particular, electrode materials[62,63] and ceramic electrolytes (e.g., $Li_{1+x}Al_xTi_{2-x}(PO_4)_3$, $Li_{1.5}Al_{0.5}Ge_{1.5}(PO_4)_3$ and $Li_{0.33}La_{0.56}TiO_3$),[66–68] polymer electrolytes have been rarely analyzed by ESM,[64] but they revealed electroosmotic flow as the dominant contribution to the observed ESM signal in PVdF-based polymers.[64] Figures 6A–6C show the AFM topography and the ESM and QNM images, respectively. While the topography (Figure 6A) exhibits a typical structure for polymeric surfaces, the ESM (Figure 6B) clearly shows regions with higher and lower ionic strain (strain induced by ion motion). This observation is attributed to (local) variations in ion mobility/ion flow within the electrolyte, where weaker signals correlate to reduced Li ion diffusion within the observed sample volume, despite that the obtained features are related to the morphology of the material. A larger-scale image of the polymer confirms these observations while also indicating a direct correlation to the heterogeneous polymer distribution at the surface (Figure S10). Within the blend-type SIPE, three different regions can be identified. Areas that display a relatively weak signal response are colored blue and occur as large, round clusters of ~200 nm and may be attributed to sample volumes containing high amounts of non-Li^+-conducting PVdF-HFP. These regions are surrounded by channel-like structures of ~20–100 nm width that are irregularly distributed on the sample surface and exhibit a strong signal response, reflecting superior Li-ion percolation paths (red), likely attributed to a rather ideal composition of SIPE and plasticizer. In between, areas with medium response are detected (green/yellow). Overall, these observations are in excellent agreement with the domain sizes of structures monitored by Raman spectroscopy, thereby verifying the reliability of both techniques. Hence, ESM mapping exhibits evidence about local strains, contributing important information to develop an optimized Li-electrolyte interface offering a rather homogeneous Li-ion deposition.

As the mechanical properties of the material may also influence the local ionic mobility, these characteristics are probed by using the QNM mode (the

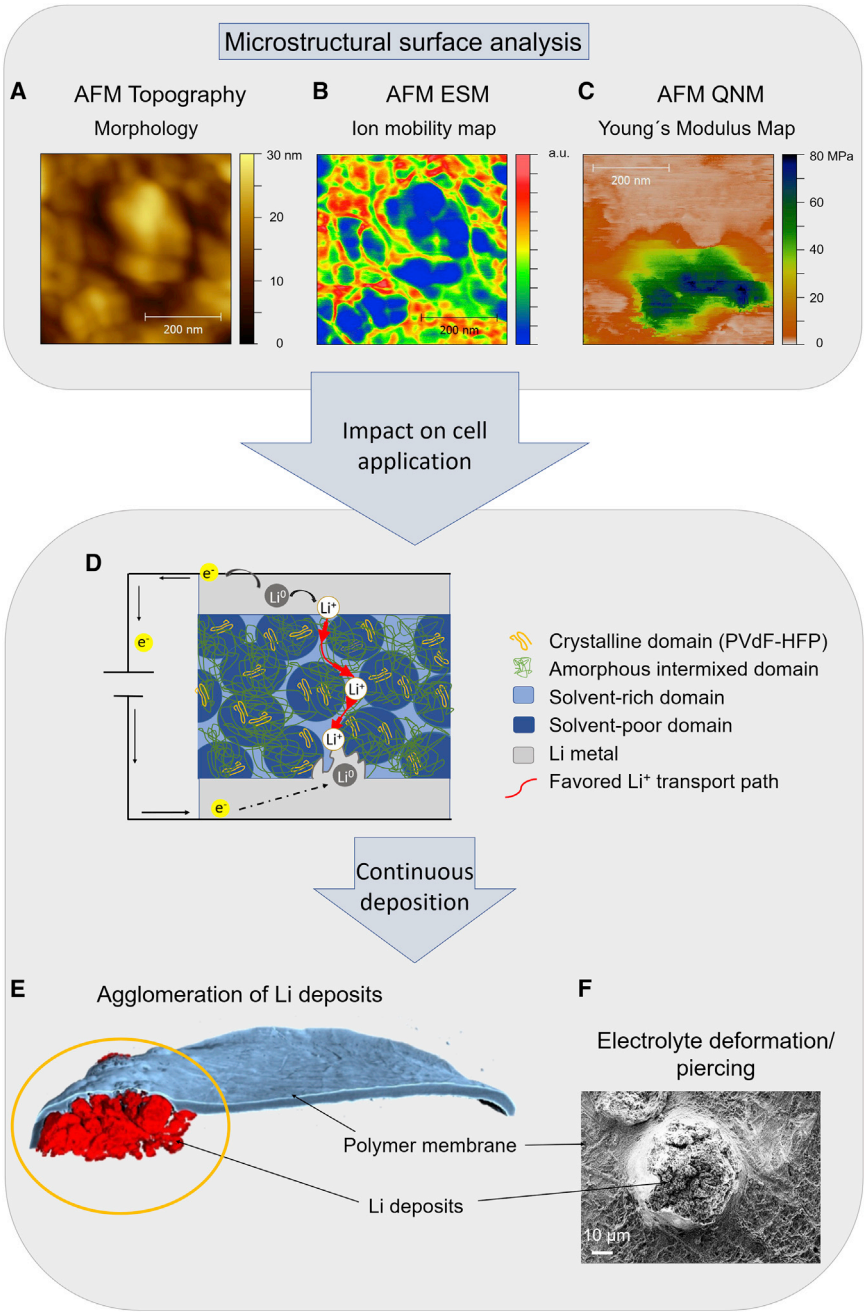

Figure 6. Schematic presentation of the Li deposition behavior

(A–C) AFM investigations: (A) AFM topography, (B) ESM mode, and (C) QNM mode.

(D) Schematics illustrating compounds of the blend polymer membrane and inhomogeneous Li deposition generated as a result of favored transport channels within the SIPE.

(E) 3D rendering of X-ray tomography of a cell in which 0.46 mg Li was plated on the anode side, applying 0.1 mA cm^{-2} for 20 h.

(F) SEM image of an agglomerated Li deposit that has penetrated the polymer membrane.

corresponding topography image is presented in Figure S11). Two different Young's moduli are obtained as shown in Figure 6C, reflecting different components in the polymer membranes. The embedded structures exhibit significantly enlarged Young's moduli of 30–80 MPa compared to the substrate with values <1 MPa.

However, the obtained value of the substrate is in reasonable agreement with data from rheometry experiments (Figure S7), yielding a stiffness on the order of 0.1 MPa for the bulk material. These results reveal various inhomogeneities on the polymer membrane surface (2D), reflecting the presence of preferential Li-ion transport channels with different width and connectivity/tortuosity, as well as dead ends within the polymer matrix (3D). While previous reports on ion (H^+, Li^+) transport in polymeric structures[20–22] reported the occurrence of distributed properties, thus far, this phenomenon has not been correlated to any consequences in electrochemical cell application—in this case, Li deposition behavior in LMBs. Here, as schematically presented in Figures 6D–6F, Li deposition and growth of deposits take place at particular spots of the Li-metal electrode. This phenomenon is promoted by the morphology of the membrane since phase separation induces a distribution of properties (ionic mobility and Young's moduli) in the polymer blend membrane. Overall, this deposition behavior significantly reduces the long-term cycling stability of the cell since agglomeration of deposits strongly stresses the membrane in these regions, thereby thinning and even perforating the membrane. This effect is comparable to the preferential growth of Li deposits along grain boundaries in ceramic electrolytes.[10]

In light of all of the obtained results, the strong deviations of theoretical and experimental value of τ_{SC} can be explained. It is plausible to conclude that τ_{SC} obtained from Chazalviel's model or other quantities derived from various models[7,8,69,70] that are based on the assumptions of homogeneous electrolytes and bulk properties is basically overestimated in view of practical results, in which transport and mechanical properties are distributed over the sample surface and volume. To approach the experimentally obtained limiting values based on theoretical calculations, a homogeneity factor, which may be calculated by the mean and standard variation of relevant parameters (e.g., Li^+ diffusion, D_{Li^+}; transference number, t^+; elastic moduli, E; shear moduli, G) should be included. However, accurate and highly resolved determination of the distribution of these decisive properties within a polymer membrane constitutes a formidable challenge, even more so when considering that materials design strategies are confronted by conflicting demands of electrochemical performance, costs, and environmental friendliness of the materials' constituents.

Despite that Li deposition homogeneity was considered a major factor for preventing Li dendrite growth in LMBs—for example, in terms of Li surface roughness,[4,24] SEI,[71] or separator properties (wetting/porosity)[4,72]—in the case of polymer electrolytes, the impact of a distribution of the chemical (micro-) environments or constituent polymer blocks remained unexplored. Phase-separated structures containing ion-conducting and structure-determining domains[73] such as block copolymers or polymer blends were often deliberately fabricated to yield favorable bulk properties (ionic conductivity, mechanical stability) while exploiting materials adaptability with respect to the necessities of intended applications. Therefore, the challenge for future electrolyte design and development consists in compromising the conflicting demands of achieving excellent bulk properties (which can be achieved by phase separation) and homogeneous morphological features based on spatially homogeneous distributions of ion transport and mechanical properties. Implementation of detailed studies of the local properties of electrolytes and Li^+ ion pathways (including transport in confined channels), in addition to the elucidation of correlations between processing parameters (e.g., utilization of different chain or block lengths of polymers, applied temperatures, amount of solvent and chemical interactions and electrolyte compounds; in the case of solution-based processing) and Li^+ ion transport networks, are considered essential for the further development of

reliable and ideally commercially viable strategies to control the resulting network/channel structures and bulk materials properties. The existence of favored transport channels can be understood as a critical but powerful design parameter, such that defined characteristics of the Li^+ transport paths by tortuosity control (e.g., short paths lengths and avoidance of dead ends, optimization of path widths for unhindered Li-ion movement, and generation of as many as possible paths of equal lengths with low deviation between the channel properties) can be explicitly used to not only boost the achievable Li^+-ion transport properties in polymer electrolytes but also control Li deposition behavior. In addition, to further homogenize the Li-ion flux on Li-metal (or Cu current collector in case of anode-free LMBs) electrodes for systems in which phase separation occurs, multi-layered polymer systems may be considered, including homogeneous, Li-ion conductive (single-compound) artificial SEI layer(s) on the electrodes.[12,74] This way, controlled and homogeneous Li deposition on the electrodes can be achieved.

The obtained results and design recommendations are also valuable in terms of unraveling the origins and preventing the formation of "orphaned"/"dead" Li. The orphaning of Li is a pivotal phenomenon occurring when non-uniformly formed and localized Li deposits lose contact, thereby significantly contributing to irreversible Li losses during cycling (in case of non-symmetric cell setups; e.g., Li||Cu or Li||-transition metal oxide cathode material).[75,76] While previous publications identified electrode architecture and interphase characteristics as potential causes for Li orphaning,[75,76] inhomogeneity of the electrolyte membrane most probably constitutes another factor inducing the formation of orphaned Li. In fact, non-uniform deposition has been widely recognized as a bottleneck in metal-based batteries also beyond Li (e.g., Zn,[77,78] Al[77]), highlighting the generic relevance of the results of this study. Applying the complementary characterization approach introduced here to other Li-based cell setups (e.g., Li||Cu for the determination of irreversible Li losses during cycling) and to other cell chemistries (e.g., Na, Zn, Al, Mg) constitutes a promising strategy to gain comprehensive knowledge of stripping/plating phenomena in metal-based batteries.

In summary, a SIPE was used to unravel Li deposition behavior and underlying crucial factors. Combining electrochemical and various optical and spectroscopic techniques, we demonstrated that the ability of (single-ion conducting) polymer electrolytes to prevent rather inhomogeneous Li-metal deposition can be controlled by its morphology, in particular, the membrane homogeneity. SEM and X-ray tomography analyses revealed that independent of the applied current density, dense (non-dendritic) Li deposits agglomerate and grow at preferential spots, eventually resulting in the deformation and penetration of polymer membranes based on high local stresses within the phase-separated domains. The intrinsic phase separation in the considered polymer membrane derived from Raman mapping induces an inhomogeneous distribution of membrane characteristics such as ionic flows (ESM) and mechanical properties (QNM) that evoke the generation of several preferential pathways for Li^+ transport that are responsible for observed deposition behavior rather than bulk electrolyte properties. While the analysis was performed for a representative polymer blend system, all of the obtained insights are generically applicable to all types of (quasi-) solid electrolytes (either dual-ion or single-ion conducting) that exhibit morphological features (domains), including blend-type polymers, block copolymers, and hybrid electrolytes beyond Li-metal chemistries (e.g., Na, Zn, Al, Mg). Our findings provide insights that promote a comprehensive understanding of Li deposition behavior and associated determining factors, specifically introducing the distribution of Li^+ ion transport properties within an electrolyte as a critical

design parameter for electrolyte development. In view of future investigations, we emphasize focusing on compromising optimized bulk properties (high ionic conductivity and high elastic modulus, which can be readily achieved by phase separation attempts) on one side and homogeneous microstructures and narrow distributions of properties to attain rather homogeneous Li deposition during cycling (thus longevity of Li-metal-based cells) on the other side. Therefore, correlations between electrolyte processing parameters with morphological features (tortuosity, channel widths and their distributions and standard deviations, presence of dead ends) and finally with Li deposition behavior should be established. Such insight may guide pathways for future electrolyte design, in principle allowing the tailoring of structural features and characteristics of Li transport channels, including (better) control of Li deposition behavior. Beyond that, interface/interphase design (e.g., application of a homogenously ion conducting [polymeric] artificial SEI) constitutes another key strategy for likely achieving controlled Li deposition in Li-metal-based cells.

EXPERIMENTAL PROCEDURES

Resource availability

Lead contact

Further information and requests for resources should be directed to and will be fulfilled by the lead contact, Gunther Brunklaus (g.brunklaus@fz-juelich.de).

Materials availability

This study did not generate new unique reagents.

Data and code availability

Raw data are available upon reasonable request from the lead contact.

Polymer membrane fabrication

Synthesis of the SIPE and preparation of the polymer membrane were performed as described in our previous work.[40] Figure S1 depicts the process of membrane fabrication. Blend polymer membranes were prepared by casting and subsequent drying of a 75-wt% SIPE and a 25-wt% PVdF-HFP solution. The dried membrane was then swollen in a mixture of ethylene carbonate (EC) and propylene carbonate (PC) (1:1, v:v) yielding a weight uptake (wt%) of 130 wt% related to the weight of the dry membrane.

Li treatment

For analysis of the impact of Li treatment on the cycling performance (overvoltages and cell lifetime) and SEI composition, Li-metal was treated as follows. Case 1: the as-received Li-metal (500 μm, Albemarle) was rinsed 3 times in anhydrous hexane (>95%, dried over activated alumina in a Pure Solv PS-MD-4-EN solvent purification system (Innovative Technology). Case 2: the as-received Li-metal was pressed between two siliconized polyester foils (PPI Adhesive Products) in 25 μm steps using a tabletop roll-press (Hohsen Corp., HSAM-615H) to a final thickness of 300 μm to reduce the surface roughness and achieve a defined surface.[26]

Characterization methods and sample preparation

Galvanostatic cycling was performed in symmetric Li|SIPE|Li coin cells (2032 type) on a battery analysis system Maccor 4000. For all of the experiments, the cells were placed in a climate chamber at a constant temperature of 60°C, where they were kept at open-circuit voltage (OCV) for 12 h before cycling.

The SEI composition was examined by XPS (AXIS Ultra DLD [Krato]) and a monochromatic Al Kα source (hV = 1,486.6 eV) at a 10-mA filament current and a 12-kV filament voltage source energy. Samples were prepared in a dry room (H_2O < 0.02%, dewpoint below −65°C) and transferred to the device without exposure to ambient atmosphere. To avoid charging the sample, a charge neutralizer was used. A 0° angle of emission and a pass energy of 20 eV were applied. Three measurements were recorded for each sample at different spots. CasaXPS software was used for spectral fitting of the obtained spectra; the binding energy of the C-C/C-H peak of the C 1 s spectra was set to 284.6 eV for calibration.

Storage and loss moduli $G'(\omega)$ and $G''(\omega)$ were determined with an Anton Paar MCR 102 device with 10-mm parallel plates. Sample dimensions were 10 mm in diameter and 70 μm thick. All of the measurements were conducted at a low strain rate of 0.1% (plateau of deformation-dependent moduli) as a function of applied angular frequency at 20°C, 40°C, and 60°C.

Samples analyzed by X-ray tomography were punched from cell stacks (Li|SIPE|Li) of disassembled and cycled coin cells (Figure S2B). The samples were punched to a sample size of 3-mm diameter from a location between the center and edge of the cell, as shown in Figure S2A. The samples were then placed horizontally inside sample containers that are tailored for X-ray tomography and made of polyether ether ketone (PEEK, Quadrant GmbH), as detailed in Figure S2C.[79] To fully exploit the field of view, three samples were stacked inside the PEEK housing (Figure S2C). Except for the rubber rings, the containers were further glued (at the level of the rubber ring) on both ends to avoid moisture penetration from ambient atmosphere. Sample packing was performed in a dry room (H_2O < 0.02%, with dewpoint below −65°C). Synchrotron X-ray tomography was performed at DESY (Germany) at P05 beamline.[80] Monochromatic X-rays ($\Delta E/E \approx 10^{-2}$) with an energy of 20 keV were used, which were generated from a double multilayer monochromator (DMM). A monochromatic beam was directed onto the sample during a 180° sample rotation. The detector consists of a 100-μm-thick $CdWO_4$ single crystal scintillator, a set of microscope optics, and a KIT CMOS camera with a CMV 20000 sensor. The applied field of view was 3.28 × 2.46 mm^2 (length × height), with a pixel size of 0.6 μm. All of the tomography datasets contain 2,400 projections with an exposure time of 0.16 s for each projection. The obtained raw image datasets were normalized, filtered, and reconstructed using in-house reconstruction software programmed by Julian Moosmann written in MATLAB.[81–83] Three-dimensional images were rendered by VGStudio MAX 3.1.

Raman spectra were recorded on a Senterra Raman spectrometer (Bruker Optics), using a laser wavelength of 785 nm and a 100× objective (numerical aperture [NA] = 0.9). The Raman spectra were recorded in a spectral range of 80–1,520 cm^{-1} with a resolution of 3–5 cm^{-1}, and the laser power was adjusted to 25 mW. For collection of the spectra, 5 integrations were carried out at an integration time of 100 s. Raman mapping was performed by applying a grid of 10 × 10 measurement points in the x- and y-directions. The distance $\Delta x/\Delta y$ between 2 measurement points was set to 200 nm, even though the calculated lateral resolution (Raleigh criterion) is 532 nm. Note that based on previous work,[84] the best information is achieved from mapping with data increments considerably smaller than the actual resolution. The Raman spectra were baseline corrected in OPUS software (Bruker Optics). To compensate for intensity variations between spectra obtained from different measurement points and to consider that compounds may be distributed inhomogeneously on the surface, characteristic peaks of the solvent solution and the single-ion conducting polymer were normalized to the integral of the whole spectrum using Origin 2016 software.

Attenuated total reflection Fourier transform infrared (ATR-FTIR) spectroscopy was performed on a Bruker Vertex 70 with a spectral resolution of 1 cm^{-1} in a spectral range between 400 and 4,000 cm^{-1} and 512 scans.

SEM was performed on a Zeiss Auriga electron microscope (Carl Zeiss Microscopy GmbH) with an accelerating voltage of 3 kV.

AFM images were recorded on a Dimension ICON (Bruker Optics) applying two different modes. For the measurements of topography and mechanical properties, the Peak Force QNM mode was used. A Bruker SCANASYST-AIR cantilever (Bruker Optics) with a calibrated spring constant of 0.28 N/m was used. For the determination of Young's modulus, a tip radius of 12 nm was assumed, and all of the parameters were validated on the corresponding Bruker reference sample kit. The (ESM mode is suitable for the qualitative detection of local variations in ionic mobility. A Bruker SCM-PIT-V2 cantilever with conductive Pt/Ir coating and a calibrated spring constant of 2.33 N/m was used. The contact resonance frequency and the amplitude were tracked with a phase-locked loop (HF2LI, Zurich Instruments). The starting/center contact resonance frequency was 267 kHz and a drive bias of 4 V AC and −2 V direct current (DC) was used; the image was scanned at a rate of 0.4 Hz. The QNM measurements were done at an AFM at ambient conditions, while the ESM measurements were conducted at a device placed inside a glove box (MBraun) that may slightly influence the amount of plasticizer contained within the sample.

SUPPLEMENTAL INFORMATION

Supplemental information can be found online at https://doi.org/10.1016/j.xcrp.2021.100496.

ACKNOWLEDGMENTS

The authors gratefully acknowledge the generous support of this collaborative work by the German Federal Ministry of Education and Research (BMBF) projects "Festbatt" (grant no. 13XP0175A), "AReLiS" (grant no. 13XP0229B), and "Benchbatt" (grant no. 03XP0047B). The authors acknowledge DESY (Hamburg, Germany), a member of the Helmholtz Association HGF, for the provision of the experimental facilities. Parts of this research were carried out at P05 beamline, PETRA III. Special thanks are offered to Dr. Fabian Wilde for help during the tomography beamtime at DESY, Na Min for help with the tomographic data analysis, Debbie Berghus for the XPS measurements, and Nino Schön for help with the ESM experiments.

AUTHOR CONTRIBUTIONS

Concept, K.B., G.B., and J.R.N.; methodology, K.B. (synthesis, SEM, and electrochemical measurements), B.W., F.H., R.-A.E. (AFM, ESM, and QNM), and K.D. and I.M. (X-ray tomography); writing – original draft, K.B.; writing – review & editing, K.D., J.R.N., G.B., I.M., F.H., and M.W.; supervision, G.B. and M.W.

DECLARATION OF INTERESTS

The authors declare no competing interests.

Received: April 28, 2021
Revised: June 11, 2021
Accepted: June 16, 2021
Published: July 13, 2021

REFERENCES

1. Schmuch, R., Wagner, R., Hörpel, G., Placke, T., and Winter, M. (2018). Performance and cost of materials for lithium-based rechargeable automotive batteries. Nat. Energy *3*, 267–278.
2. Betz, J., Bieker, G., Meister, P., Placke, T., Winter, M., and Schmuch, R. (2019). Theoretical versus Practical Energy: A Plea for More Transparency in the Energy Calculation of Different Rechargeable Battery Systems. Adv. Energy Mater. *9*, 1–18.
3. Albertus, P., Babinec, S., Litzelman, S., and Newman, A. (2018). Status and challenges in enabling the lithium metal electrode for high-energy and low-cost rechargeable batteries. Nat. Energy *3*, 16–21.
4. Shen, X., Liu, H., Cheng, X.B., Yan, C., and Huang, J.Q. (2018). Beyond lithium ion batteries: higher energy density battery systems based on lithium metal anodes. Energy Storage Mater. *12*, 161–175.
5. Winter, M., Barnett, B., and Xu, K. (2018). Before Li Ion Batteries. Chem. Rev. *118*, 11433–11456.
6. Placke, T., Kloepsch, R., Dühnen, S., and Winter, M. (2017). Lithium ion, lithium metal, and alternative rechargeable battery technologies: the odyssey for high energy density. J. Solid State Electrochem. *21*, 1939–1964.
7. Chazalviel, J. (1990). Electrochemical aspects of the generation of ramified metallic electrodeposits. Phys. Rev. A *42*, 7355–7367.
8. Monroe, C., and Newman, J. (2005). The impact of elastic deformation on deposition kinetics at lithium/polymer interfaces. J. Electrochem. Soc. *152*, 396–404.
9. Harry, K.J., Higa, K., Srinivasan, V., and Balsara, N.P. (2016). Influence of Electrolyte Modulus on the Local Current Density at a Dendrite Tip on a Lithium Metal Electrode. J. Electrochem. Soc. *163*, A2216–A2224.
10. Janek, J., and Zeier, W.G. (2016). A solid future for battery development. Nat. Energy *1*, 1–4.
11. Harry, K.J., Hallinan, D.T., Parkinson, D.Y., MacDowell, A.A., and Balsara, N.P. (2014). Detection of subsurface structures underneath dendrites formed on cycled lithium metal electrodes. Nat. Mater. *13*, 69–73.
12. Lopez, J., Mackanic, D.G., Cui, Y., and Bao, Z. (2019). Designing polymers for advanced battery chemistries. Nat. Rev. Mater. *4*, 312–330.
13. Tikekar, M.D., Archer, L.A., and Koch, D.L. (2016). Stabilizing electrodeposition in elastic solid electrolytes containing immobilized anions. Sci. Adv. *2*, e1600320.
14. Bieker, G., Winter, M., and Bieker, P. (2015). Electrochemical in situ investigations of SEI and dendrite formation on the lithium metal anode. Phys. Chem. Chem. Phys. *17*, 8670–8679.
15. Li, Z., Huang, J., Yann Liaw, B., Metzler, V., and Zhang, J. (2014). A review of lithium deposition in lithium-ion and lithium metal secondary batteries. J. Power Sources *254*, 168–182.
16. Cheng, X.B., Zhang, R., Zhao, C.Z., and Zhang, Q. (2017). Toward Safe Lithium Metal Anode in Rechargeable Batteries: A Review. Chem. Rev. *117*, 10403–10473.
17. Gireaud, L., Grugeon, S., Laruelle, S., Yrieix, B., and Tarascon, J.M. (2006). Lithium metal stripping/plating mechanisms studies: a metallurgical approach. Electrochem. Commun. *8*, 1639–1649.
18. Tikekar, M.D., Archer, L.A., and Koch, D.L. (2014). Stability Analysis of Electrodeposition across a Structured Electrolyte with Immobilized Anions. J. Electrochem. Soc. *161*, A847–A855.
19. Barton, J.L. (1962). The electrolytic growth of dendrites from ionic solutions. Proc. R. Soc. Lond. A Math. Phys. Sci. *268*, 485–505.
20. Webb, M.A., Jung, Y., Pesko, D.M., Savoie, B.M., Yamamoto, U., Coates, G.W., Balsara, N.P., Wang, Z.G., and Miller, T.F., 3rd (2015). Systematic computational and experimental investigation of lithium-ion transport mechanisms in polyester-based polymer electrolytes. ACS Cent. Sci. *1*, 198–205.
21. Kambe, Y., Arges, C.G., Czaplewski, D.A., Dolejsi, M., Krishnan, S., Stoykovich, M.P., de Pablo, J.J., and Nealey, P.F. (2019). Role of Defects in Ion Transport in Block Copolymer Electrolytes. Nano Lett. *19*, 4684–4691.
22. Hou, J., Li, J., Mountz, D., Hull, M., and Madsen, L.A. (2013). Correlating morphology, proton conductivity, and water transport in polyelectrolyte-fluoropolymer blend membranes. J. Membr. Sci. *448*, 292–299.
23. Xu, W., Wang, J., Ding, F., Chen, X., Nasybulin, E., Zhang, Y., and Zhang, J.G. (2014). Lithium metal anodes for rechargeable batteries. Energy Environ. Sci. *7*, 513–537.
24. Ryou, M.H., Lee, Y.M., Lee, Y., Winter, M., and Bieker, P. (2015). Mechanical surface modification of lithium metal: towards improved Li metal anode performance by directed Li plating. Adv. Funct. Mater. *25*, 834–841.
25. Bhatt, A.I., Kao, P., Best, A.S., and Hollenkamp, A.F. (2013). Understanding the Morphological Changes of Lithium Surfaces during Cycling in Electrolyte Solutions of Lithium Salts in an Ionic Liquid. J. Electrochem. Soc. *160*, A1171–A1180.
26. Becking, J., Gröbmeyer, A., Kolek, M., Rodehorst, U., Schulze, S., Winter, M., Bieker, P., and Stan, M.C. (2017). Lithium-Metal Foil Surface Modification: An Effective Method to Improve the Cycling Performance of Lithium-Metal Batteries. Adv. Mater. Interfaces *4*, 1700166.
27. Lin, D., Liu, Y., Liang, Z., Lee, H.W., Sun, J., Wang, H., Yan, K., Xie, J., and Cui, Y. (2016). Layered reduced graphene oxide with nanoscale interlayer gaps as a stable host for lithium metal anodes. Nat. Nanotechnol. *11*, 626–632.
28. Park, J., Jeong, J., Lee, Y., Oh, M., Ryou, M.H., and Lee, Y.M. (2016). Micro-Patterned Lithium Metal Anodes with Suppressed Dendrite Formation for Post Lithium-Ion Batteries. Adv. Mater. Interfaces *3*, 1–9.
29. Schmitz, P., Kolek, M., Diddens, D., Stan, M.C., Jalkanen, K., Winter, M., and Bieker, P. (2017). Counterintuitive trends of the wetting behavior of ionic liquid-based electrolytes on modified lithium electrodes. Phys. Chem. Chem. Phys. *19*, 19178–19187.
30. Zhang, M., Becking, J., Stan, M.C., Lenoch, A., Bieker, P., Kolek, M., and Winter, M. (2020). Wetting phenomena and their effect on the electrochemical performance of surface-tailored lithium metal electrodes in contact with cross-linked polymeric electrolytes. Angew. Chem. Int. Ed. Engl. *59*, 17145–17153.
31. Bhattacharyya, R., Key, B., Chen, H., Best, A.S., Hollenkamp, A.F., and Grey, C.P. (2010). In situ NMR observation of the formation of metallic lithium microstructures in lithium batteries. Nat. Mater. *9*, 504–510.
32. Chang, H.J., Trease, N.M., Ilott, A.J., Zeng, D., Du, L.-S., Jerschow, A., and Grey, C.P. (2015). Investigating Li Microstructure Formation on Li Anodes for Lithium Batteries by In Situ 6Li/ 7Li NMR and SEM. J. Phys. Chem. C *119*, 16443–16451.
33. Bai, P., Li, J., Brushett, F.R., and Bazant, M.Z. (2016). Transition of lithium growth mechanisms in liquid electrolytes. Energy Environ. Sci. *9*, 3221–3229.
34. Brissot, C., Rosso, M., Chazalviel, J.-N., and Lascaud, S. (1999). Dendritic growth mechanisms in lithium/polymer cells. J. Power Sources *81–82*, 925–929.
35. Chang, H.J., Ilott, A.J., Trease, N.M., Mohammadi, M., Jerschow, A., and Grey, C.P. (2015). Correlating Microstructural Lithium Metal Growth with Electrolyte Salt Depletion in Lithium Batteries Using ^{7}Li MRI. J. Am. Chem. Soc. *137*, 15209–15216.
36. Zhang, Y., Rohan, R., Cai, W., Xu, G., Sun, Y., Lin, A., and Cheng, H. (2014). Influence of chemical microstructure of single-ion polymeric electrolyte membranes on performance of lithium-ion batteries. ACS Appl. Mater. Interfaces *6*, 17534–17542.
37. Chen, Y., Ke, H., Zeng, D., Zhang, Y., Sun, Y., and Cheng, H. (2017). Superior polymer backbone with poly(arylene ether) over polyamide for single ion conducting polymer electrolytes. J. Membr. Sci. *525*, 349–358.
38. Rohan, R., Sun, Y., Cai, W., Zhang, Y., Pareek, K., Xu, G., and Cheng, H. (2014). Functionalized polystyrene based single ion conducting gel polymer electrolyte for lithium batteries. Solid State Ion. *268*, 294–299.
39. Martinez-Ibañez, M., Sanchez-Diez, E., Qiao, L., Zhang, Y., Judez, X., Santiago, A., Aldalur, I., Carrasco, J., Zhu, H., Forsyth, M., et al. (2020). Unprecedented Improvement of Single Li-Ion Conductive Solid Polymer Electrolyte Through Salt Additive. Adv. Funct. Mater. *30*, 1–9.
40. Borzutzki, K., Thienenkamp, J., Diehl, M., Winter, M., and Brunklaus, G. (2019). Fluorinated polysulfonamide based single ion conducting room temperature applicable gel-type polymer electrolytes for lithium ion

batteries. J. Mater. Chem. A Mater. Energy Sustain. *7*, 188–201.

41. Bruce, G., and Vincent, A. (1987). Steady state current flow in solid binary electrolyte cells. J. Electroanal. Chem. Interfacial Electrochem. *225*, 1–17.

42. Khurana, R., Schaefer, J.L., Archer, L.A., and Coates, G.W. (2014). Suppression of lithium dendrite growth using cross-linked polyethylene/poly(ethylene oxide) electrolytes: a new approach for practical lithium-metal polymer batteries. J. Am. Chem. Soc. *136*, 7395–7402.

43. Liu, K., Bai, P., Bazant, M.Z., Wang, C.A., and Li, J. (2017). A soft non-porous separator and its effectiveness in stabilizing Li metal anodes cycling at 10 mA cm−2 observed in situ in a capillary cell. J. Mater. Chem. A Mater. Energy Sustain. *5*, 4300–4307.

44. Gungor, M.R., Watkins, J.J., and Maroudas, D. (2008). Mechanical behavior of ultralow-dielectric-constant mesoporous amorphous silica. Appl. Phys. Lett. *92*, 251903.

45. Trapa, P.E., Huang, B., Won, Y.Y., Sadoway, D.R., and Mayes, A.M. (2002). Block copolymer electrolytes synthesized by atom transfer radical polymerization for solid-state, thin-film lithium batteries. Electrochem. Solid-State Lett. *5*, 85–88.

46. Bouchet, R., Maria, S., Meziane, R., Aboulaich, A., Lienafa, L., Bonnet, J.P., Phan, T.N.T., Bertin, D., Gigmes, D., Devaux, D., et al. (2013). Single-ion BAB triblock copolymers as highly efficient electrolytes for lithium-metal batteries. Nat. Mater. *12*, 452–457.

47. Oikonomou, E.K., Tencé-Girault, S., Gérard, P., and Norvez, S. (2015). Swelling of semi-crystalline PVDF by a PMMA-based nanostructured diblock copolymer: morphology and mechanical properties. Polymer (Guildf.) *76*, 89–97.

48. Kalaw, G.J.D., Wahome, J.A.N., Zhu, Y., Balkus, K.J., Musselman, I.H., Yang, D.J., and Ferraris, J.P. (2013). Perfluorocyclobutyl (PFCB)-based polymer blends for proton exchange membrane fuel cells (PEMFCs). J. Membr. Sci. *431*, 86–95.

49. Barlow, J.W. (1993). Polymer blends and alloys. Makromol. Chem. Macromol. Symp. *70-71*, 235–244.

50. Dixit, M.B., Zaman, W., Hortance, N., Chen, C., Balke, N., Hatzell, K.B., Dixit, M.B., Zaman, W., Hortance, N., Vujic, S., et al. (2020). Nanoscale Mapping of Extrinsic Interfaces in Hybrid Solid Electrolytes Nanoscale Mapping of Extrinsic Interfaces in Hybrid Solid Electrolytes. Joule *4*, 207–221.

51. Borzutzki, K., Dong, D., Wölke, C., Kruteva, M., Stellhorn, A., Winter, M., Bedrov, D., and Brunklaus, G. (2020). Small Groups, Big Impact: Eliminating Li^+ Traps in Single-Ion Conducting Polymer Electrolytes. iScience *23*, 101417.

52. Tchitchekova, D.S., Monti, D., Johansson, P., Bardé, F., Randon-Vitanova, A., Palacín, M.R., and Ponrouch, A. (2017). On the Reliability of Half-Cell Tests for Monovalent (Li +, Na +) and Divalent (Mg 2+, Ca 2+) Cation Based Batteries. J. Electrochem. Soc. *164*, A1384–A1392.

53. Allen, J.L., Borodin, O., Seo, D.M., and Henderson, W.A. (2014). Combined quantum chemical/Raman spectroscopic analyses of Li+ cation solvation: Cyclic carbonate solvents - ethylene carbonate and propylene carbonate. J. Power Sources *267*, 821–830.

54. Gouadec, G., Bellot-Gurlet, L., Baron, D., and Colomban, P. (2012). Raman Imaging. Techniques and Applications (Springer).

55. Jeschke, S., Mutke, M., Jiang, Z., Alt, B., and Wiemhöfer, H.D. (2014). Study of carbamate-modified disiloxane in porous PVDF-HFP membranes: new electrolytes/separators for lithium-ion batteries. ChemPhysChem *15*, 1761–1771.

56. Peleš, A., Aleksić, O., Pavlović, V.P., Djoković, V., Dojčilović, R., Nikolić, Z., Marinković, F., Mitrić, M., Blagojević, V., Vlahović, B., et al. (2018). Structural and electrical properties of ferroelectric poly(vinylidene fluoride) and mechanically activated ZnO nanoparticle composite films. Phys. Scr. *93*, 105801.

57. Arabnejad, S., Yamashita, K., and Manzhos, S. (2017). Defects in crystalline PVDF: a density functional theory-density functional tight binding study. Phys. Chem. Chem. Phys. *19*, 7560–7567.

58. Parker, A., Ueda, A., Ce, M., and Sk, H. (2018). Structural and Thermal Treatment Evaluation of Electrospun PVDF Nanofibers. J. Polym. Sci. A *2*, 5–8.

59. Riosbaas, M.T., Loh, K.J., O'Bryan, G., and Loyola, B.R. (2014). In situ phase change characterization of PVDF thin films using Raman spectroscopy. In Proceedings of the Sensors and Smart Structures Technologies for Civil, Mechanical, and Aerospace Systems, *9061* (SPIE).

60. Sharma, M., Madras, G., and Bose, S. (2014). Process induced electroactive β-polymorph in PVDF: effect on dielectric and ferroelectric properties. Phys. Chem. Chem. Phys. *16*, 14792–14799.

61. Zhao, D., Martinelli, A., Willfahrt, A., Fischer, T., Bernin, D., Khan, Z.U., Shahi, M., Brill, J., Jonsson, M.P., Fabiano, S., and Crispin, X. (2019). Polymer gels with tunable ionic Seebeck coefficient for ultra-sensitive printed thermopiles. Nat. Commun. *10*, 1093.

62. Balke, N., Jesse, S., Morozovska, A.N., Eliseev, E., Chung, D.W., Kim, Y., Adamczyk, L., García, R.E., Dudney, N., and Kalinin, S.V. (2010). Nanoscale mapping of ion diffusion in a lithium-ion battery cathode. Nat. Nanotechnol. *5*, 749–754.

63. Balke, N., Kalnaus, S., Dudney, N.J., Daniel, C., Jesse, S., and Kalinin, S.V. (2012). Local detection of activation energy for ionic transport in lithium cobalt oxide. Nano Lett. *12*, 3399–3403.

64. Romanyuk, K., Costa, C.M., Luchkin, S.Y., Kholkin, A.L., and Lanceros-Méndez, S. (2016). Giant Electric-Field-Induced Strain in PVDF-Based Battery Separator Membranes Probed by Electrochemical Strain Microscopy. Langmuir *32*, 5267–5276.

65. Proksch, R. (2011). Electrochemical Strain Microscopy of Li-ion Conductive Materials for Energy Generation and Storage. http://react.rutgers.edu/~huixinhe/courses/scanprobemicro/Electrochemical%20Strain%20Microscopy.pdf.

66. Schön, N., Schierholz, R., Jesse, S., Yu, S., Eichel, R.A., Balke, N., and Hausen, F. (2021). Signal Origin of Electrochemical Strain Microscopy and Link to Local Chemical Distribution in Solid State Electrolytes. Small Methods *5*, 2001279.

67. Schön, N., Gunduz, D.C., Yu, S., Tempel, H., Schierholz, R., and Hausen, F. (2018). Correlative electrochemical strain and scanning electron microscopy for local characterization of the solid state electrolyte $Li_{1.3}Al_{0.3}Ti_{1.7}(PO_4)_3$. Beilstein J. Nanotechnol. *9*, 1564–1572.

68. Yu, J., Duan, S., Huang, B., Jin, H., Xie, S., and Li, J. (2020). Spatially Resolved Electrochemical Strain of Solid-State Electrolytes via High Resolution Sequential Excitation and Its Implication on Grain Boundary Impedance. Small Methods *4*, 1–8.

69. Monroe, C., and Newman, J. (2003). Dendrite Growth in Lithium/Polymer Systems: A Propagation Model for Liquid Electrolytes under Galvanostatic Conditions. J. Electrochem. Soc. *150*, A1377–A1384.

70. Rosso, M., Gobron, T., Brissot, C., Chazalviel, J.N., and Lascaud, S. (2001). Onset of dendritic growth in lithium/polymer cells. J. Power Sources *97–98*, 804–806.

71. Hao, F., Verma, A., and Mukherjee, P.P. (2018). Mechanistic insight into dendrite-SEI interactions for lithium metal electrodes. J. Mater. Chem. A Mater. Energy Sustain. *6*, 19664–19671.

72. Lagadec, M.F., Zahn, R., and Wood, V. (2019). Characterization and performance evaluation of lithium-ion battery separators. Nat. Energy *4*, 16–25.

73. Nguyen, H.-D., Kim, G.-T., Shi, J., Paillard, E., Judenstein, P., Lyonnard, S., Bresser, D., and Iojoiu, C. (2018). Nanostructured multi-block copolymer single-ion conductors for safer high-performance lithium batteries. Energy Environ. Sci. *11*, 3298–3309.

74. Liu, B., Zhang, J.G., and Xu, W. (2018). Advancing Lithium Metal Batteries. Joule *2*, 833–845.

75. Zheng, J., Kim, M.S., Tu, Z., Choudhury, S., Tang, T., and Archer, L.A. (2020). Regulating electrodeposition morphology of lithium: towards commercially relevant secondary Li metal batteries. Chem. Soc. Rev. *49*, 2701–2750.

76. Zheng, J., Tang, T., Zhao, Q., Liu, X., Deng, Y., and Archer, L.A. (2019). Physical Orphaning versus Chemical Instability: Is Dendritic Electrodeposition of Li Fatal? ACS Energy Lett. *4*, 1349–1355.

77. Zheng, J., Bock, D.C., Tang, T., Zhao, Q., Yin, J., Tallman, K.R., Wheeler, G., Liu, X., Deng, Y., Jin, S., et al. (2021). Regulating electrodeposition morphology in high-capacity aluminium and zinc battery anodes using interfacial metal–substrate bonding. Nat. Energy *6*, 398–406.

78. Zheng, J., and Archer, L.A. (2021). Controlling electrochemical growth of metallic zinc

electrodes: toward affordable rechargeable energy storage systems. Sci. Adv. *7*, 1–20.

79. Dong, K., Osenberg, M., Sun, F., Markötter, H., Jafta, C.J., Hilger, A., Arlt, T., Banhart, J., and Manke, I. (2019). Non-destructive characterization of lithium deposition at the Li/separator and Li/carbon matrix interregion by synchrotron X-ray tomography. Nano Energy *62*, 11–19.

80. Wilde, F., Ogurreck, M., Greving, I., Hammel, J.U., Beckmann, F., Hipp, A., Lottermoser, L., Khokhriakov, I., Lytaev, P., Dose, T., et al. (2016). Micro-CT at the imaging beamline P05 at PETRA III. In AIP Conference Proceedings, *1741* (American Institute of Physics).

81. Moosmann, J., Ershov, A., Weinhardt, V., Baumbach, T., Prasad, M.S., LaBonne, C., Xiao, X., Kashef, J., and Hofmann, R. (2014). Time-lapse X-ray phase-contrast microtomography for in vivo imaging and analysis of morphogenesis. Nat. Protoc. *9*, 294–304.

82. van Aarle, W., Palenstijn, W.J., Cant, J., Janssens, E., Bleichrodt, F., Dabravolski, A., De Beenhouwer, J., Joost Batenburg, K., and Sijbers, J. (2016). Fast and flexible X-ray tomography using the ASTRA toolbox. Opt. Express *24*, 25129–25147.

83. van Aarle, W., Palenstijn, W.J., De Beenhouwer, J., Altantzis, T., Bals, S., Batenburg, K.J., and Sijbers, J. (2015). The ASTRA Toolbox: a platform for advanced algorithm development in electron tomography. Ultramicroscopy *157*, 35–47.

84. Guan, P., Liu, L., and Lin, X. (2015). Simulation and experiment on solid electrolyte interphase (SEI) morphology evolution and lithium-ion diffusion. J. Electrochem. Soc. *162*, A1798–A1808.